Research Article | Vol. 26, No. 4 | 19 Feb 2018 | OPTICS EXPRESS 4330
Optics EXPRESS

Integrated polar microstructure and template-matching method for optical position measurement

CHENYANG ZHAO, CHIFAI CHEUNG,* AND MINGYU LIU

Partner State Key Laboratory of Ultra-precision Machining Technology, Department of Industrial and Systems Engineering, The Hong Kong Polytechnic University, Hung Hom, Kowloon, Hong Kong, China
**benny.cheung@polyu.edu.hk*

Abstract: This paper presents an integrated polar microstructure and template-matching method for optical position measurement that is developed based on the technology of ultra-precision machining (UPM) and computer vision. For computer vision, this paper makes use of the template-matching method as the basic working principle to match the position on the surface. For UPM, an optical microstructure that is named a 'polar microstructure' is purposely designed and fabricated by ultra-precision diamond machining technology to provide the high resolution of the position measurement. To demonstrate the performance of the proposed method for optical position measurement, a high-precision multi-sensor coordinate measuring machine was used to test the position accuracy and the length uncertainty for the two axes of this positioning method. The experimental results show that the average length uncertainty and the corresponding standard deviation errors are 109.6 nm and 76.4 nm on the X-axis, and 91.8 nm and 69.7 nm on the Y-axis, respectively.

OCIS codes: (120.0120) Instrumentation, measurement, and metrology; (120.6650) Surface measurements, figure.

References and links

1. T. A. M. Ruijl, "Ultra precision coordinate measuring machine-design, calibration and error compensation," (2001).
2. E. Solecky, O. D. Patterson, A. Stamper, E. McLellan, R. Buengener, A. Vaid, C. Hartig, B. Bunday, A. Arceo, and A. Cepler, "In-line E-beam wafer metrology and defect inspection: the end of an era for image-based critical dimensional metrology? New life for defect inspection," Proc. SPIE **8681**, 86810D (2013).
3. T. Castenmiller, F. van de Mast, T. de Kort, C. van de Vin, M. de Wit, R. Stegen, and S. van Cleef, "Towards ultimate optical lithography with NXT: 1950i dual stage immersion platform," in *Proc. SPIE*, 2010), 76401N.
4. W. Gao, S. Kim, H. Bosse, H. Haitjema, Y. Chen, X. Lu, W. Knapp, A. Weckenmann, W. Estler, and H. Kunzmann, "Measurement technologies for precision positioning," CIRP Annals-Manufacturing Technology **64**(2), 773–796 (2015).
5. T. Oiwa, M. Katsuki, M. Karita, W. Gao, S. Makinouchi, K. Sato, and Y. Oohashi, "Questionnaire survey on ultra-precision positioning," Int. J. Automot. Technol. **5**(6), 766–772 (2011).
6. C. Wong, C. Montes, L. Mears, and J. Ziegert, "A new position feedback method for manufacturing equipment," Algorithms **1**, 4 (2008).
7. C. Y. Wong, C. Montes, L. Mears, and J. Ziegert, "Model-based control to enhance a novel two dimensional positioning system," in Control Automation and Systems (ICCAS), 2010 International Conference on, (IEEE, 2010), 19–22.
8. C. A. Montes, C. Wong, J. C. Ziegert, and L. Mears, "Vision-based tracking of a dynamic target with application to multi-axis position control," J. Real-Time Image Process. **10**(1), 119–134 (2015).
9. X. Li, W. Gao, H. Muto, Y. Shimizu, S. Ito, and S. Dian, "A six-degree-of-freedom surface encoder for precision positioning of a planar motion stage," Precis. Eng. **37**(3), 771–781 (2013).
10. W. Gao, "Surface Encoder for Measurement of In-plane Motion," Precision Nanometrology: Sensors and Measuring Systems for Nanomanufacturing, 69–108 (2010).
11. C.-C. Wu, Y.-Z. Chen, and C.-H. Liao, "Common-path laser planar encoder," Opt. Express **21**(16), 18872–18883 (2013).
12. V. Guelpa, P. Sandoz, M. A. Vergara, C. Clévy, N. Le Fort-Piat, and G. J. Laurent, "2D visual micro-position measurement based on intertwined twin-scale patterns," Sens. Actuators A Phys. **248**, 272–280 (2016).
13. Z.-H. Chen and P. S. Huang, "A vision-based method for planar position measurement," Meas. Sci. Technol. **27**(12), 125018 (2016).

#309283 https://doi.org/10.1364/OE.26.004330
Journal © 2018 Received 16 Oct 2017; revised 28 Jan 2018; accepted 2 Feb 2018; published 9 Feb 2018

Optics EXPRESS

14. C. Zhao, C. F. Cheung, and M. Liu, "Modeling and Simulation of a Machining Process Chain for the Precision Manufacture of Polar Microstructure," Micromachines (Basel) **8**(12), 345 (2017).
15. C. Zhao, C. Cheung, and L. Kong, "A study of optimization of machining strategy for enhancing the efficiency of process chain in ultra-precision machining," euspen's 16th International Conference & Exhibition, Nottingham, UK. (2016).
16. R. Brunelli, *Template-matching Techniques in Computer Vision: Theory and Practice* (John Wiley & Sons, 2009).
17. R. Brunelli and T. Poggio, "Face recognition: Features versus templates," IEEE Trans. Pattern Anal. Mach. Intell. **15**(10), 1042–1052 (1993).
18. B. M. Quine, V. Tarasyuk, H. Mebrahtu, and R. Hornsey, "Determining star-image location: A new sub-pixel interpolation technique to process image centroids," Comput. Phys. Commun. **177**(9), 700–706 (2007).
19. X. Jiang, X. Zhang, and P. J. Scott, "Template-matching of freeform surfaces based on orthogonal distance fitting for precision metrology," Meas. Sci. Technol. **21**(4), 045101 (2010).
20. E. Cuevas, V. Osuna, and D. Oliva, *Evolutionary Computation Techniques: A Comparative Perspective* (Springer, 2017), Vol. **686**.
21. D. Keren, S. Peleg, and R. Brada, "Image sequence enhancement using sub-pixel displacements," in Computer Vision and Pattern Recognition, 1988. Proceedings CVPR'88., Computer Society Conference on, (IEEE, 1988), 742–746.
22. M. Debella-Gilo and A. Kääb, "Sub-pixel precision image matching for measuring surface displacements on mass movements using normalized cross-correlation," Remote Sens. Environ. **115**(1), 130–142 (2011).
23. H. Nobach, N. Damaschke, and C. Tropea, "High-precision sub-pixel interpolation in particle image velocimetry image processing," Exp. Fluids **39**(2), 299–304 (2005).

1. Introduction

Precision measurement has been widely applied in many areas such as dimensional measuring instruments [1], machine tools [2], semiconductor manufacturing equipment [3], and so on. Currently, there are many fundamental optical sensor technologies applied in precision measurement [4]. For example, time-of-flight distance sensors and absolute laser interferometer sensors have a high resolution with micrometer to nanometer accuracy, and a fairly long measurement range. As air refractive index error and wavelength error are their main uncertainty source, a strict environment such us vacuum is needed to control the above uncertainty source. Optical encoders are the most widely used sensors for precision positioning in production engineering [5–8] and the most famous working principle used is the periodic pattern such as sine planar encoder followed by estimation of its phase change to calculate the position change through a series of Fourier transforms [9–11]. Based on this principle, many research studies in pattern-based vision for precision measurement have been investigated [12, 13]. The above research idea has a strict condition which is that the manufacturing error of pattern must be tiny. If the error of pattern becomes large, the corresponding phase estimation is inaccurate. Furthermore, there has been a common thought that it is necessary for the key components of measurement equipment to undergo calibration first, but the calibration is time-consuming and needs additional machines to validate it. A series of research has been previously investigated [14, 15], and this paper attempts to directly use fabricated surfaces as the standard reference, no matter whether with machining errors, owing to the fabrication principle of the surface named polar microstructure which is discussed in Chapter 3 as well as template-matching using computer vision.

Template-matching in image processing is used for the detection and recognition of objects from their images, irrespective of their orientation, scale, and view, and is a very important research area in computer vision [16]. It has been used in many areas such as face recognition [17], and it is also used to determine the star-image location [18] which is similar to precision position measurement, the difference being that one is for macro size while the other is for micro size. The template-matching method has been developed in macro area, while only relatively little research in precision measurement used a similar theory. However, the definition of their template-matching method is different for optical image processing [19]. The reason why little research was studied the micro area is not only the difficulties of crossing research areas but also due to the difficulty to distinguish the target with sufficient features. Most structures appear to have a high similarity when they are shown in a

Optics EXPRESS

microscope, but if there is a structure which still has distinguished features everywhere even at the micrometer level, it would require great integration of the template-matching method and UPM technology. This paper presents a feasible way to integrate two research areas together so as to achieve precision position measurement. A flowchart is provided in Fig. 1.

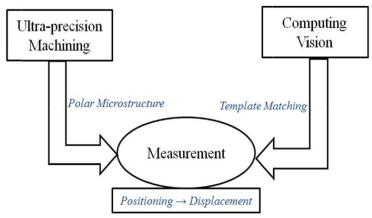

Fig. 1. Flowchart of the core idea in this paper.

In this paper, the definitions of pixel and optical intensity are firstly introduced, then the theory of template-matching in image processing is described. Further, a sub-pixel resolution method using Bilinear Interpolation is developed to improve the resolution and accuracy of the template-matching method. A novel microstructure named 'polar microstructure' was fabricated by ultra-precision diamond machining technology as a searching map for the template-matching method. Lastly, a series of experiments was conducted to verify the accuracy of the template-matching method for precision positioning measurement.

2. Theory

2.1 Pixel and optical intensity

Computer vision can be considered as the science and technology of machines that obtain information from images which are created by the interaction of light with objects. Light is actually a propagating oscillatory disturbance in the electromagnetic field whose wave equation can be expressed as Eq. (1):

$$(\nabla^2 - \frac{1}{c}\frac{\partial^2}{\partial t^2})E = 0 \tag{1}$$

where ∇^2 is the Laplace operator, c is the speed of light, E is the electric field and light is a visible solution of Eq. (1).

Even if light is described by using the wave equation, there are no sensors to detect directly its amplitude and phase. The only quantity that can be detected is the intensity I of the radiation incident on the sensor. As a result, the intensity I is a key parameter to obtain and describe the light properties instead of the light amplitude and phase which are difficult to be obtained. Moreover, for a plane wave, the light intensity I is proportional to E^2 which is described as Eq. (2):

$$I(x_1, x_2) \propto E^2 \tag{2}$$

where (x_1, x_2) represents a point on the surface at which the measurement is performed.

However, (x_1, x_2) is a point in a mathematical sense. Actually, there must be a term to describe the characteristics of the point (x_1, x_2), which is named 'pixel'.

In digital imaging, a pixel is the smallest controllable element of an image represented on a screen. Each pixel is a sample of an original image, and the optical intensity I of each pixel varies where more samples are typically provided a higher representation of the original

image. As a result, the point (x_1, x_2) is represented by the pixel (u, v) under actual circumstances.

On the whole, the core idea of this paper is to make use of sensors (i.e. industrial cameras, microscopes, etc.) as the data acquisition tool to observe the physical objects (i.e. polar microstructure). The feature information of the objects is acquired by the sensor through the propagation of light; the senor preserves the intensity information of the physical objects in the forms of grayscale images. In essence, a grayscale image is a two-dimensional array $A(m \times n)$:

$$\begin{bmatrix} a_{11} & a_{12} & \cdots & a_{1n} \\ a_{21} & a_{22} & \cdots & a_{2n} \\ \cdots & \cdots & \cdots & \cdots \\ a_{m1} & a_{m2} & \cdots & a_{mn} \end{bmatrix}_{m \times n} .$$

The number (m, n) refers to the row and the column of the two-dimensional array which represents the number of the pixels in the vertical (m) and horizontal (n) directions of the grayscale image. The value of the element a_{uv} in the array represents the intensity value I of the pixel (u, v).

2.2 Template-matching

The first step aims to illustrate some terms. Template image (T) is the given image which is compared to other images and it is expected that there is an image that most matches the template image (T). According to the previous description in section 2.1, template image (T) can be described as a two-dimensional array $T_{m \times n}$:

$$\begin{bmatrix} t_{11} & t_{12} & \cdots & t_{1n} \\ t_{21} & t_{22} & \cdots & t_{2n} \\ \cdots & \cdots & \cdots & \cdots \\ t_{m1} & t_{m2} & \cdots & t_{mn} \end{bmatrix}_{m \times n} .$$

where m is the number of the pixels in the vertical direction of the template image (T), n is the number of the pixels in the horizontal direction of template image (T), and t_{uv} represents the intensity value I of the pixel (u, v) in template image (T).

Global image (G) is a larger-sized image which offers a global map for the subsequent searching and in which template image (T) is expected to find a match.. Similarly, global image (G) is described as $G_{M \times N}$:

$$\begin{bmatrix} g_{11} & g_{12} & \cdots & g_{1N} \\ g_{21} & g_{22} & \cdots & g_{2N} \\ \cdots & \cdots & \cdots & \cdots \\ g_{M1} & g_{M2} & \cdots & g_{MN} \end{bmatrix}_{M \times N} ..$$

where M is the number of the pixels in the vertical direction of global image (G), N is the number of pixels in the horizontal direction of global image (G), and g_{uv} represents the intensity value I of the pixel (u, v) in global image (G).

Reference image (R) is the real-time image which is a part of global image (G) and moves along the horizontal and vertical direction in global image (G) by each pixel step. Reference image (R) is defined as $R_{m\times n}$:

$$\begin{bmatrix} r_{11} & r_{12} & \cdots & r_{1n} \\ r_{21} & r_{22} & \cdots & r_{2n} \\ \cdots & \cdots & \cdots & \cdots \\ r_{m1} & r_{m2} & \cdots & r_{mn} \end{bmatrix}_{m\times n} .$$

where m is the number of the pixels in the vertical direction of reference image (R), n is the number of pixels in the horizontal direction of reference image (R), and r_{uv} represents the intensity value I of the pixel (u,v) in reference image (R). It is noted that the size of R is the same as that of T ; it aims to find the position where R has the most similarity to T .

To illustrate the template-matching process clearly, Fig. 2 shows the principle of template-matching, and the small black area is regarded as one pixel. In global image G ($M\times N$ pixels), reference image R ($m\times n$ pixel) moves across the search area ($(M-m)\times(N-n)$ pixels) with each pixel along the x and y axes respectively, $R_{(1,1)}$ is the starting reference image, $R_{(u,v)}$ is the reference image which shifts to u^{th} and v^{th} pixels of global image G in the x and y directions respectively, and $R_{(M-m,N-n)}$ is the ending reference image. In each move step, a similarity between R and T is calculated. On the whole, a template-matching problem can be illustrated as: given template image T and global image G , find the position (u,v) within the search region where the similarity between reference image $R_{u,v}(x,y)$ and template image (T) is the maximum.

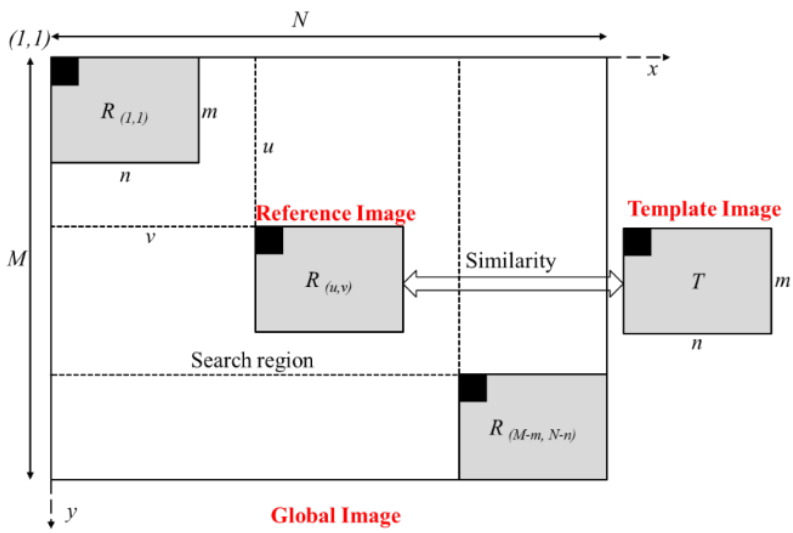

Fig. 2. Principle of template-matching.

The next step is to determine how to indicate the similarity value between R and T . The Normalized Cross-Correlation (NCC) method has been proven to be one of the most effective and robust methods that support the measurement of the resemblance between T and its coincident region at image R [20]. The NCC value is given by Eq. (3):

Optics EXPRESS

$$NCC_{(u,v)} = \frac{\sum_{i=1}^{m}\sum_{j=1}^{n}[R(u+i,v+j)-\bar{R}(u,v)]\cdot[T(i,j)-\bar{T}]}{\left[\sum_{i=1}^{m}\sum_{j=1}^{n}(R(u+i,v+j)-\bar{R}(u,v))^2\right]^{\frac{1}{2}}\cdot\left[\sum_{i=1}^{m}\sum_{j=1}^{n}(T(i,j)-\bar{T})^2\right]^{\frac{1}{2}}} \quad (3)$$

where $\bar{R}(u,v)$ is the grayscale average intensity of reference image $R(u,v)$, whereas $\bar{T}$ is the grayscale average intensity of template image T. These values are defined as Eq. (4) and Eq. (5):

$$\bar{R}(u,v) = \frac{1}{m\cdot n}\sum_{i=1}^{m}\sum_{j=1}^{n}R(u+i,v+j) \quad (4)$$

$$\bar{T} = \frac{1}{m\cdot n}\sum_{i=1}^{m}\sum_{j=1}^{n}T(i,j) \quad (5)$$

The NCC values are delivered between the interval [-1, 1], which means that if NCC = 1 the similarity is the best possible, whereas if NCC = −1 the template and the corresponding image are completely different. As a result, the point (u,v) which presents the best possible resemblance between R and T is defined as Eq. (6) and Eq. (7):

$$(u,v) = \arg\max_{(\hat{u},\hat{v})\in A} NCC(\hat{u},\hat{v}) \quad (6)$$

where,

$$A = \{(u,v)\,|\,1\le\hat{u}\le M-m, 1\le\hat{v}\le N-n\} \quad (7)$$

2.3 Sub-pixel interpolation

The issue of sub-pixel estimation appears because the available images are often not at the optimal resolution for precision quantification of movement. Currently, there are many interpolation methods in the image processing area such as Bi-cubic interpolation, Parabolic interpolation, Gaussian interpolation, etc [18, 21–23]. In this study, the Bilinear Interpolation (BI) method was used. After interpolation, the theoretical resolution of the template-matching method improves from 1 pixel to $1/(k_{Inter}+1)$ pixel, where k_{Inter} is the number of interpolation points in a single pixel.

3. Manufacturing of the polar microstructure

Since the template-matching method has been used to determine star position in the field of astronomy as mentioned above, considering the similarity of macroscopic and microcosmic levels, the template-matching method is also feasible for precision positioning measurement. Although the principle for template-matching has been developed, sup-pixel interpolation is also able to improve its theoretical distinguishing resolution, while there is a prime difficulty in the development of template-matching in precision measurement, that is, how to make global image G have remarkable features everywhere even in a microscope. In other words, let the NCC value difference of each search area in a microscope or industry camera be as much as possible. This difficulty is also the prime reason why the template-matching method has not been widely used in the precision measurement area.

In this paper, UPM is used to solve this problem. It should be noticed that UPM is not used primarily for controlling the machining error, but to improve the remarkable features of machined surface. Based on the above, a novel polar microstructure is proposed to solve this problem. Figure 3 shows the design and manufacture of polar microstructure.

Optics EXPRESS

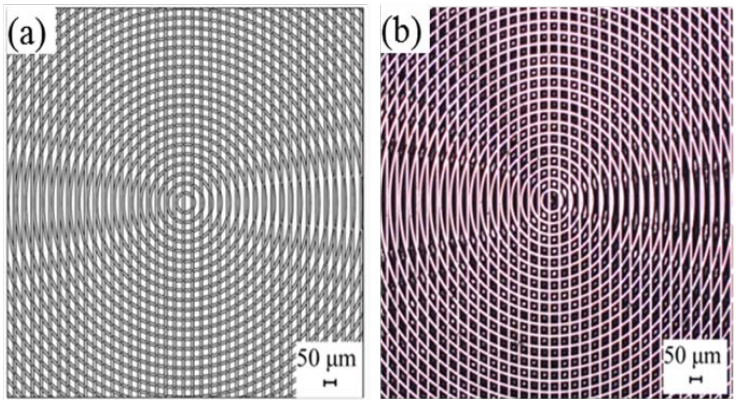

Fig. 3. Polar microstructure. 1) Design model 2) Machining results measured with a Pearl Centering Microscope.

The polar microstructure looks like a polar coordinate. It is fabricated by the UPM process chain combined with single point diamond turning and diamond broaching on the ultra-precision machine Nanoform 350G from Nanotechnology Inc., USA. The surface feature of the polar microstructure is composed of concentric circles and straight lines whose spacing is equal to 50 micrometers, respectively.

Firstly, it is found that the polar microstructure possesses a high discrimination rate even though the form accuracy is in the micrometer range. Usually, the visual field of a microscope or industrial camera is larger than 100 μm × 100 μm. An arbitrary area of this size in the polar microstructure is different. In other words, its grayscale intensity distribution is unique. To illustrate this clearly, this paper gives an example to explain the details. Figure 4 shows three images captured on polar microstructure surface by the Zygo Nexview 3D Optical Surface Profiler (Zygo, Middlefield, CT, USA). Three pictures were chosen as reference images (R), and the image shown in Fig. 4(a) was chosen as template image (T). The actual display size of each photo is 100 μm × 100 μm (160 pixels × 160 pixels). Figure 4(a) was captured on the central area of the polar microstructure, Fig. 4(b) was captured along the horizontal centerline of the polar microstructure and Fig. 4(c) was captured at a random point of the polar microstructure.

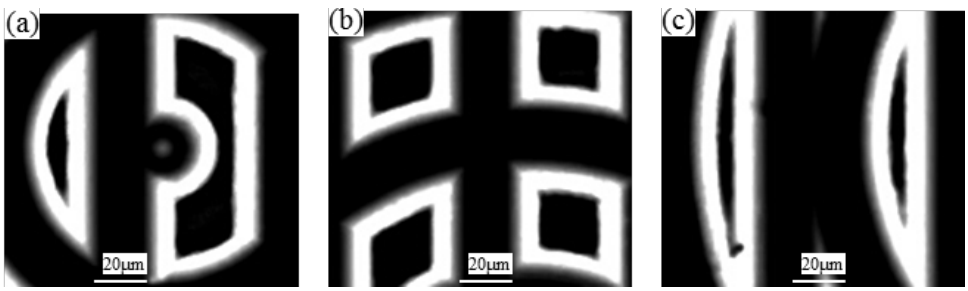

Fig. 4. Comparison of the differences among the reference images captured on polar microstructure.

As abovementioned in the theory of template-matching, the image shown in Fig. 4(a) was chosen as both template image and reference image, and can be expressed as Eq. (8) and Eq. (9):

$$T = R(a) \tag{8}$$

Optics EXPRESS

$$R(a)=\begin{bmatrix} 254 & 255 & \cdots & 0 & 0 \\ 255 & 251 & & 0 & 0 \\ \cdots & & \begin{matrix} 38 & 44 \\ 56 & 61 \end{matrix} & \cdots & \\ 255 & 253 & & 0 & 0 \\ 255 & 252 & \cdots & 0 & 0 \end{bmatrix}_{160\times160} \tag{9}$$

where $R(a)$ represents the reference image which is Fig. 4(a).

According to Eq. (3), its NCC value is calculated by Eq. (10):

$$NCC_{(a)}=\frac{\sum_{i=1}^{160}\sum_{j=1}^{160}[R(a)-\bar{R}(a)]\cdot[T-\bar{T}]}{\left[\sum_{i=1}^{160}\sum_{j=1}^{160}(R(a)-\bar{R}(a))^2\right]^{\frac{1}{2}}\cdot\left[\sum_{i=1}^{160}\sum_{j=1}^{160}(T-\bar{T})^2\right]^{\frac{1}{2}}}=1 \tag{10}$$

where $\bar{R}(a)$ is the gray scale average intensity of reference image $R(a)$, whereas $\bar{T}$ is the gray scale average intensity of template image T.

Since the reference image is the same as the template image, its NCC value is 1. The same can be obtained with the following Eq. (11) to Eq. (14):

$$R(b)=\begin{bmatrix} 0 & 0 & \cdots & 26 & 19 \\ 0 & 0 & & 29 & 20 \\ \cdots & & \begin{matrix} 129 & 149 \\ 163 & 179 \end{matrix} & \cdots & \\ 0 & 0 & & 22 & 7 \\ 0 & 0 & \cdots & 22 & 7 \end{bmatrix}_{160\times160} \tag{11}$$

$$NCC_{(b)}=\frac{\sum_{i=1}^{160}\sum_{j=1}^{160}[R(b)-\bar{R}(b)]\cdot[T-\bar{T}]}{\left[\sum_{i=1}^{160}\sum_{j=1}^{160}(R(b)-\bar{R}(b))^2\right]^{\frac{1}{2}}\cdot\left[\sum_{i=1}^{160}\sum_{j=1}^{160}(T-\bar{T})^2\right]^{\frac{1}{2}}}=0.1302 \tag{12}$$

$$R(c)=\begin{bmatrix} 0 & 0 & \cdots & 0 & 0 \\ 0 & 0 & & 0 & 0 \\ \cdots & & \begin{matrix} 255 & 211 \\ 255 & 214 \end{matrix} & \cdots & \\ 0 & 0 & & 0 & 0 \\ 0 & 0 & \cdots & 0 & 0 \end{bmatrix}_{160\times160} \tag{13}$$

Optics EXPRESS

$$NCC_{(c)} = \frac{\sum_{i=1}^{160}\sum_{j=1}^{160}[R(c)-\bar{R}(c)]\cdot[T-\bar{T}]}{\left[\sum_{i=1}^{160}\sum_{j=1}^{160}(R(c)-\bar{R}(c))^2\right]^{\frac{1}{2}}\cdot\left[\sum_{i=1}^{160}\sum_{j=1}^{160}(T-\bar{T})^2\right]^{\frac{1}{2}}} = 0.2396 \quad (14)$$

where $R(b)$ represents the reference image which is Fig. 4(b), $R(c)$ represents the reference image which is Fig. 4(c), $\bar{R}(b)$ is the gray scale average intensity of reference image $R(b)$, and $\bar{R}(c)$ is the gray scale average intensity of reference image $R(c)$.

According to Eq. (6), the image which has the maximum NCC value can be obtained by Eq. (15):

$$\arg\max NCC(1, 0.1302, 0.2396) = 1_{R(a)} \quad (15)$$

As a result, the point at Fig. 4(a) presents the best possible resemblance between R and T. The result also shows that there is a difference in the distinctive value between the best reference location and the other reference locations. This infers that the polar microstructure is able to satisfy the requirement.

Secondly, the precision manufacturing of the polar microstructure only needs to be undertaken by a single machine tool. Since the transferring error between different machine tools can be avoided, the machining efficiency and accuracy can be high with a lower degree of machining difficulty.

Most importantly, both global image (G) and template image (T) were captured from the polar microstructure with the same microscope and under the same other conditions, which means even though there may be machining errors of the polar microstructure compared with the theoretical model, both the target (T) and the searching map (G)come from the same fabricated polar microstructure surface, so the machining errors are counteracted. Moreover, even if the illumination intensity when capturing changes constantly due to the noise, according to Eq. (3), the NCC value is calculated by the following two fractions: $[R(u+i, v+j)-\bar{R}(u,v)]$, the $[T(i,j)-\bar{T}]$ which are the difference values with the average grayscale intensity. The illumination intensity has little influence on the NCC value as well as the accuracy of this method, so the integrated polar microstructure and template-matching method prevents the noise from the light and increase the robustness.

Lastly, the requirement for the working environment of application of the method is less than that for that of the current methods such as vacuum, denoising, etc. As a result, it has a great potential for commercial production in the future.

In other words, with the help of polar microstructure and template-matching, it is easy to achieve accurate optical position measurement.

4. Experimental validations

4.1 Experimental setup

An experimental setup was built to test the integrated polar microstructure and template-matching method and obtain its uncertainty for two-axis length measurement. The experimental setup primarily consists of polar microstructure fixed on a nano-stage and observed through a microscope camera. In order to obtain convincing experimental data, the experiment bench was primarily built based on the multi-sensor coordinate measuring machine (CMM) Video-Check UA 400 3D CNC from Werth Inc., Germany as shown in Fig. 5. This CMM possesses1-nm level resolution and 0.15-μm uncertainty of length measurement. It is equipped with a camera with a resolution of 1356 pixels × 1021 pixels, a

Optics EXPRESS

pixel size of 454.200 nm in the X direction and 453.755 nm in the Y direction. The image captured by the microscope camera is shown as Fig. 5(c).

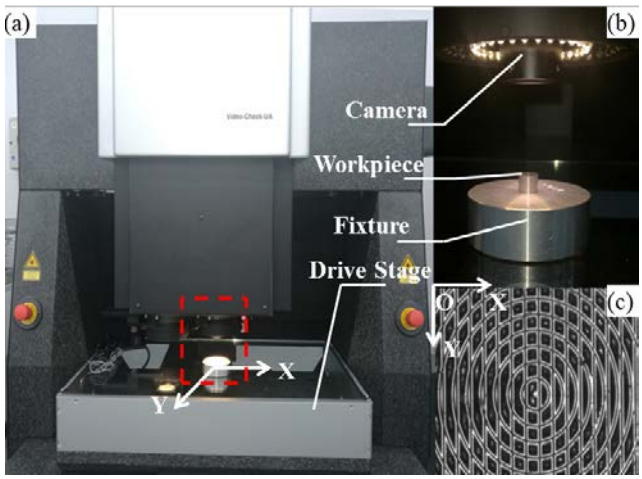

Fig. 5. Experimental setup. (a) Overall appearance (b) Magnification figure from dotted line area in Fig. 5(a) (c) Displayed image captured by the camera.

In this experiment, the image shown in Fig. 5(c) was chosen as global image G and had 1021 pixels × 1021 pixels (real size of displayed area: 463.7 μm × 463.3 μm). To test the position performance of the integrated polar microstructure and template-matching method, Fig. 6 shows the experimental procedures. The camera which is driven by the X-Y stage of the CMM moves firstly only along the X axis by 10 μm at each step, shown as the solid arrow in Fig. 6. Meanwhile, the camera captured the current image of the polar microstructure at each step to prepare for template image (T). After each 10 steps, that is, after the camera moved 100 μm along the X axis in relation to the starting point, the camera moved back to 0 μm along the X axis and moved 10 μm along the Y axis synchronously, shown as the dotted arrow. The above moving steps formed one period. The moving of the camera was repeated according to the period until it moved to the end position (X = 100 μm, Y = 100 μm) as shown in Fig. 6.

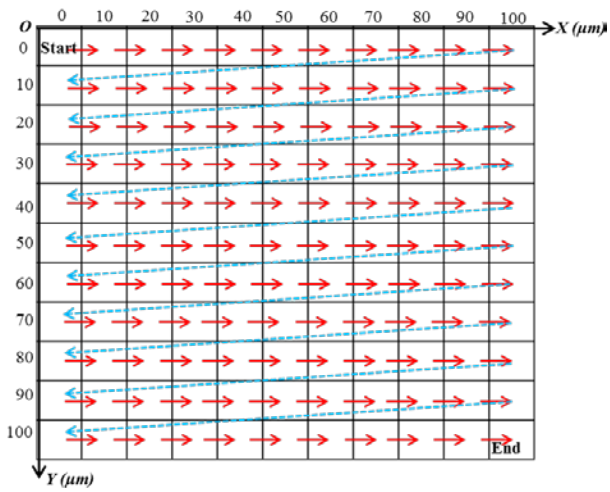

Fig. 6. Locus of moving steps of the camera.

4.2 Position errors test

Then the integrated polar microstructure and template-matching method was used to calculate the position of each image as captured by the camera at each step. It should be illustrated that considering the calculation amount in Eq. (3) as well as to prevent there being some area which was actually outside the area of global image (G), the top left corner (100 pixels × 100 pixels) of each image captured by the camera was chosen as template image (T), and when the reference image ($R_{\max}$) with the most similarity to template image (T) was calculated, the pixel (u,v) at the top left corner of $R_{\max}$ was defined as the "result pixel". The actual distance between the "result pixel" and the pixel at the top left corner of global image (G)was defined as the position. After calculation, all the calculated position points were compared to the actual position points.

Figure 7 shows a comparison between the calculated position points and actual positions by the motion stage. The top right corner of Fig. 7 shows a typical partial magnification of the result. To illustrate the measurement performance of the integrated polar microstructure and template-matching method clearly, the distance ($D_{(i,j)}$) of each measurement point between actual position coordinate value ($x_{werth(i,j)}$, $y_{werth(i,j)}$) and the calculated position coordinate value ($x_{TM(i,j)}$, $y_{TM(i,j)}$) was determined, which can be expressed as Eq. (16):

$$D_{(i,j)} = \sqrt{(x_{werth(i,j)} - x_{TM(i,j)})^2 - (y_{werth(i,j)} - y_{TM(i,j)})^2} \tag{16}$$

where $i = 0,1...10$, $j = 0,1...10$.

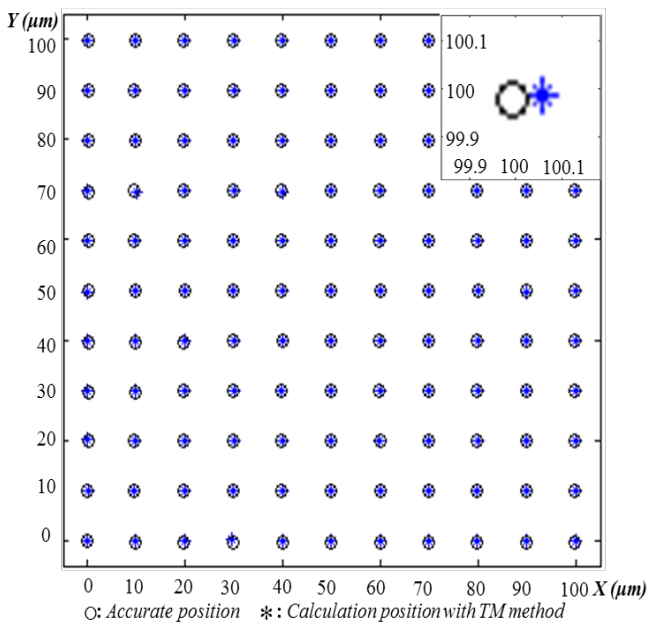

Fig. 7. Accurate and calculated positions within the area of 100 μm × 100 μm.

Figure 8 shows the error distributions in the moving area of the camera, and the average error value was found to be 257.34 nm and the maximum error value was 487.15 nm.

Optics EXPRESS

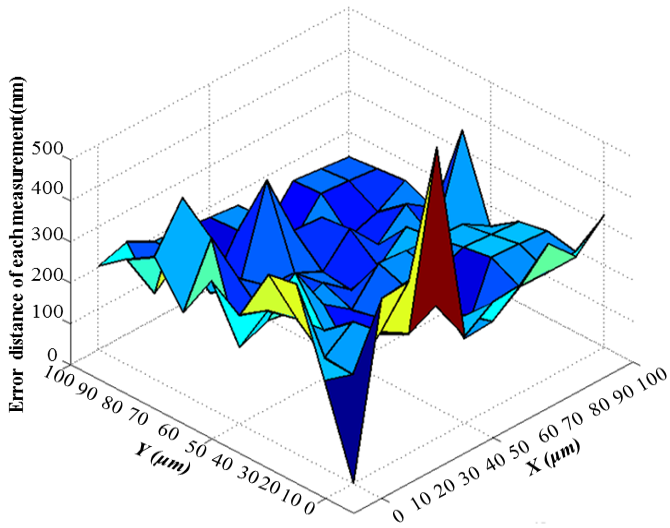

Fig. 8. Error distributions in the searching map (100 μm × 100 μm).

Figure 9 shows a theoretical analysis of the distance error distribution. As shown in Fig. 9, the square area represents an original pixel. Through the sub-pixel algorithm, the original pixel was divided into a smaller-size-level sub-pixel. During this experiment, one original pixel was divided into 32 sub-pixels along the X and Y axes respectively. As shown in Fig. 9, the original pixel was symbolically divided into some parts, and the size of the sub-pixel was the resolution value.

The template-matching algorithm was conducted in two stages. In the first stage, according to Fig. 2, the desired pixel was calculated. In most situations, the actual position is the area of the calculated pixel. Due to the size limitation of the original pixel, the current resolution was at the 400-nm level which is not acceptable, but with the help of sub-pixel interpolation, the selected pixel and its surrounding half-pixel space area were sub-pixel interpolated so as to determine the high accurate position.

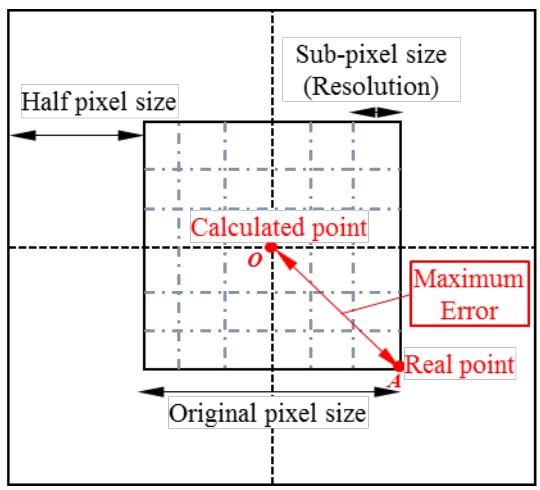

Fig. 9. Theoretical analysis of error distributions.

According to the geometrical relationship in Fig. 9, the theoretical maximum distance error between the actual position and the calculated position can be derived according to Eq. (17):

Optics EXPRESS

$$D_{\max} = \sqrt{(x_{werth(i,j)} - x_{TM(i,j)})^2 - (y_{werth(i,j)} - y_{TM(i,j)})^2}$$
$$= \sqrt{(\frac{P_x}{2})^2 + (\frac{P_y}{2})^2} \quad (17)$$
$$= \sqrt{(\frac{454.200}{2})^2 + (\frac{453.755}{2})^2} \approx 321nm$$

As shown in Fig. 8, the experimental results show that the average error value (257.34 nm) was within the maximum range (321 nm). However, among the total 121 calculated position points, there were two points whose distance error (487.15 nm and 460.77 nm) was more than the theoretical maximum error value compared to the actual position points. This is because the theoretical calculation is on the condition that the actual position point is in the selected pixel area. However, during the first template-matching calculation stage, there were some situations where the actual points were not in the selected pixel area, which caused the larger error.

4.3 Length uncertainty

To analyze its length uncertainty in each axis, the experimental data were obtained from the above experimental data as shown in Fig. 6 and Fig. 7. Each column of data has 10 measured points whose Y coordinate value is at the same level, and 10 columns were chosen from X = 10 μm to X = 100 μm. The Y output values of the abovementioned selected points are shown as Fig. 10(a). Similarly, each row of data has 10 measured points whose X coordinate value is at the same level, and 10 columns were chosen from Y = 10 μm to Y = 100 μm. The X output values of the abovementioned selected points are shown as Fig. 10(b). The experimental results show that the step motions were clearly distinguishable. The average errors and the standard deviation errors at each step were approximately 109.6 nm and 76.4 nm on the X axis, and 65.5 nm and 147.1 nm on the Y axis.

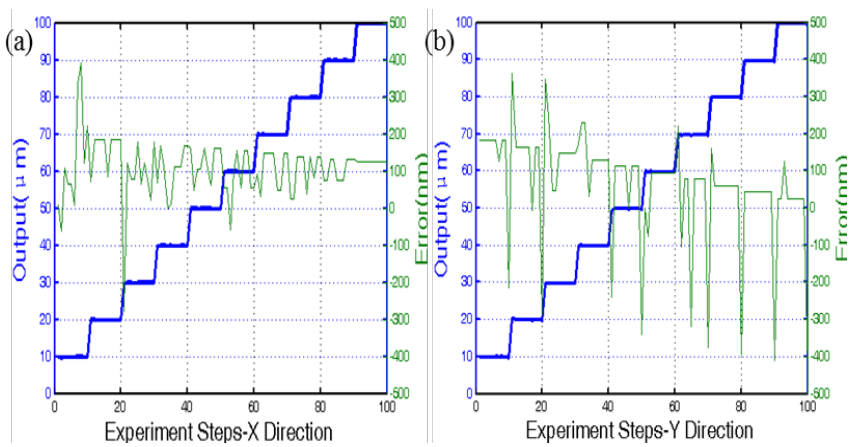

Fig. 10. Outputs and errors of step-test results. (a) 10 μm steps on the X axis (b) 10 μm steps on the Y axis.

However, from the experimental results shown as Fig. 10, it should be noticed that there seemed to be much less absolute positioning deviation in the step test results as shown in Fig. 10(a) than that in Fig. 10(b). Furthermore, as shown in Fig. 10(b), there are often 400-nm-level errors which approximately one original pixel size appeared in the last x step and the next first x step for each y step. However, there is no such obvious phenomenon shown in Fig. 10(a). This indicates that there were probably some systematic error contributions between the first and the last x step for each y step profile.

In practice, due to manufacturing and assembly errors of the workpiece, the camera may not be mounted exactly perpendicular to the surface of the workpiece, and the X axis and Y axis may not be perfectly orthogonal to each other. These are possible error sources that may affect the accuracy of the measurement, but they are not able to explain the obvious difference of positioning errors between Fig. 10(a) and Fig. 10(b). The prime reason is the experimental moving locus of the camera.

Figure 11 shows the explanation the above phenomenon. In this experiment, the camera moved consequent 10 steps along the horizontal direction (X axis) before moving along the vertical direction (Y axis). Due to the system error, there was an angle error between the X axis direction of movement of the camera. As shown in Fig. 11, Point A represents the starting moving point, and points B, C and D represent the process moving points. Points a, b, c and d are their corresponding calculated position points using the template-matching method. At first, points A, B and C were all in original pixels in the same horizontal row, but with the moving of the camera, point D fell on the pixel above the previous row. According to the algorithm, firstly, it should be determined on which original pixel the position point falls, and then the sub-pixel position on this original pixel. As shown in Fig. 11, ε_a represents the actual vertical distance between point C and point D, where ε_c represents the calculated vertical distance between points c and d. Due to the calculation uncertainty, there is a large value difference periodically between the vertical distance for two adjacent measuring points, which explains the periodic error jumping phenomenon as shown in Fig. 10 (b).

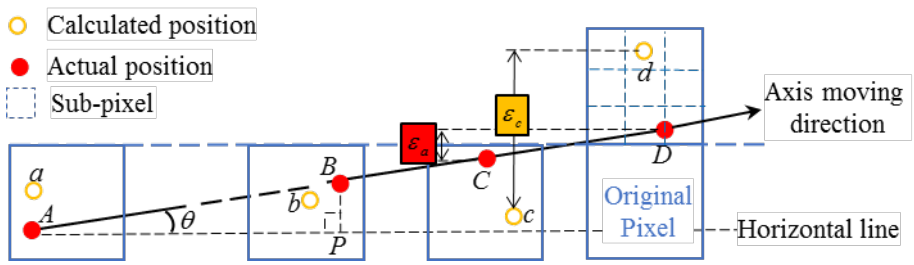

Fig. 11. Explanation of experimental results.

In Fig. 11, Eq. (18) and Eq. (19) can be derived:

$$\varepsilon_{Vertical} = BP = AB\sin\theta \tag{18}$$

$$\varepsilon_{Horizontal} = AB - AP = AB(1-\cos\theta) = \varepsilon_{Vertical}\cdot\frac{1-\cos\theta}{\sin\theta} = \varepsilon_{Vertical}\cdot\tan(\frac{\theta}{2}) \tag{19}$$

where $\varepsilon_{Vertical}$ is the system vertical error and $\varepsilon_{Horizontal}$ is the system horizontal error.

Since θ is fairly tiny, $\varepsilon_{Horizontal} << \varepsilon_{Vertical}$, which means according to the moving locus of the camera as shown in Fig. 6, the horizontal positioning error deviation is much less that in the vertical direction. This explains why Fig. 10(a) has no such obvious periodic error jumping phenomenon as in Fig. 10(b).

To validate this explanation, an additional group of control experiments was conducted. All experimental conditions were the same as in the previous experiment except the moving locus of the camera. Figure 12 shows the moving locus of the camera in the control experiment. The camera firstly moves consequent 10 steps along the vertical direction (Y axis) before moving along the horizontal direction (X axis).

Optics EXPRESS

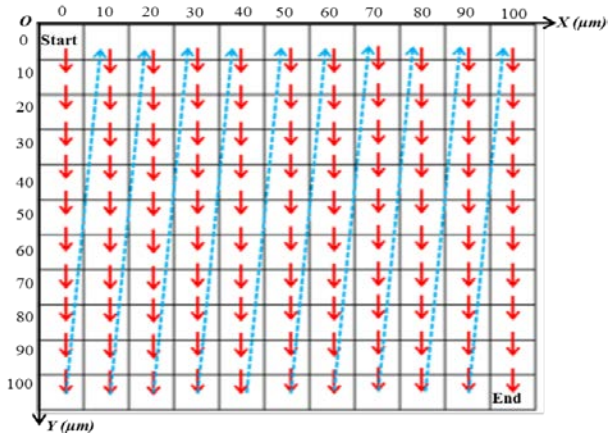

Fig. 12. Locus of moving steps of the camera in the control experiment.

The measurement results in the control experiment are shown in Fig. 13. The experimental results show that the average errors and the standard deviation errors at each step were approximately 56.3 nm and 148.9 nm on the X axis, 91.8 nm and 69.7 nm on the Y axis. It is interesting to note that the positioning error deviation in the X direction was much less than that in the Y direction. The experiment results also demonstrate that the error between the camera moving direction with absolute horizontal or vertical direction had a bad influence on the length uncertainty measurement results. To reduce the influence of system errors, it was necessary to conduct two control experiments.

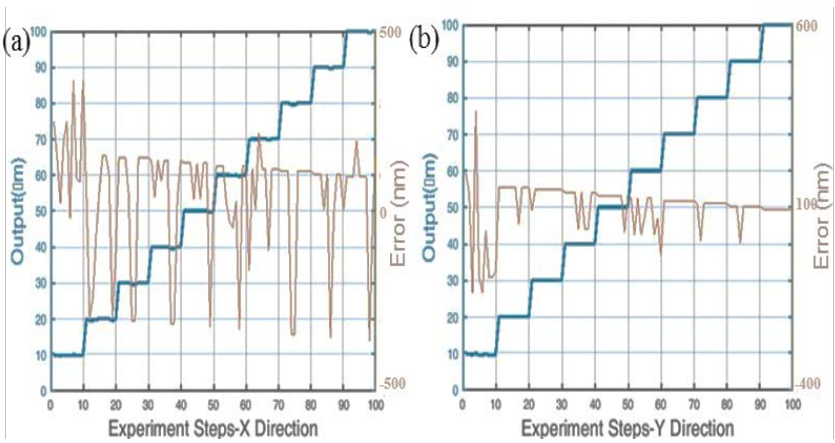

Fig. 13. Outputs and errors of step-test results in the control experiment (a) 10 μm steps on the X axis (b) 10 μm steps on the Y axis.

On the whole, the experimental results show that the integrated polar microstructure and template-matching method is at least able to achieve 100-nm-level length uncertainty. Considering this precision level, it has great potentiality for workpiece positioning on machine tools which will be further studied.

5. Limitations and future improvements

Currently, the prime challenge of the template-matching method is its calculation time: the time needed to calculate each position point is about 10 minutes by using the processor Intel(R) Core(TM) i7-6600U CPU. But there are many algorithms such as Early Jump-out and, M-estimators to speed up the template-matching calculation speed. Moreover, another efficient approach is firstly reducing the searching map of template-matching by using

Optics EXPRESS

feature point detection before template-matching calculation. One of our prime future works will focus on improving the efficiency of the template-matching method.

6. Conclusion

In this paper, a novel positioning method is presented named the integrated polar microstructure and template-matching method which has the advantages of computing vision and UPM technology. The principle of the template-matching method is used in image processing which is able to achieve 100-nm-mlevel length uncertainty provided by the polar microstructure which is fabricated by the UPM process chain composed of single point diamond turning and diamond broaching processes. The polar microstructure was purposely developed and fabricated to provide highly distinguished features in microscopes. The method was experimentally verified by the CMM which possesses10-nm-level resolution and the experimental results show that the length uncertainty of the integrated polar microstructure and template-matching method can achieve 100-nm-level resolution. Thus, its application in workpiece positioning on machine tools is feasible and worthy of being further investigated.

Funding

PhD studentship (project account code: RU7J) from The Hong Kong Polytechnic University.

Acknowledgments

The authors would like to express their sincere thanks for the support of the Partner State Key Laboratories in Hong Kong from the Innovation and Technology Commission (ITC) of the Government of the Hong Kong Special Administrative Region (HKSAR), China.